Longshore Surface Currents Measured by Doppler Radar and Video PIV Techniques

Dragana Perkovic, *Member, IEEE*, Thomas C. Lippmann, and Stephen J. Frasier, *Senior Member, IEEE*

***Abstract*—Mean longshore surface currents within the surf zone were measured using two remote sensing techniques: microwave Doppler radar and optical video. Doppler radar relies on small-scale surface roughness that scatters the incident electromagnetic radiation so that velocities are obtained from the Doppler shift of the backscattered radiation. Video relies on texture and contrast of scattered sunlight from the sea surface, and velocity estimates are determined using particle imaging velocimetry (PIV). This paper compares video PIV and Doppler radar surface velocities over a 1-km alongshore by 0.5-km cross-shore area in the surf zone of a natural beach. The two surface velocity estimates are strongly correlated ($R^2 \geq 0.79$) over much of the surf zone. Estimates differ at the outer edge of the surf where strong breaking is prevalent, with radar-estimated velocities as much as 50% below the video estimates. The radar and PIV velocities at particular locations in the surf zone track each other well over a 6-h period, showing strong modulations in the mean alongshore flow occurring on 10–20-min time intervals. In one case, both systems observe a strong eddylike mean flow pattern over a 200-m section of coastline, with the mean alongshore current changing direction at about the mid surf zone. The good spatial and temporal agreement between the two remote measurement techniques, which rely on very different mechanisms, suggests that both are reasonably approximating the true mean longshore surface velocity.**

***Index Terms*—Electromagnetic scattering, radar velocity measurement, sea surface, video signal processing.**

I. Introduction

THE PROCESSES of erosion and sediment transport determine the bathymetric evolution of natural beaches. The alongshore transport of sediments and pollutants in the surf zone is primarily driven by mean currents, with the circulation often characterized by mean longshore flows. These flows are affected by local bathymetry, as well as spatial and temporal changes in incident-wave energy and direction. The ability to capture the spatial and temporal variations in mean flows in the surf zone is key to predicting the morphological change of the nearshore topography and shoreline.

Much of the field research in the nearshore zone has been accomplished with *in situ* measurement techniques using instruments such as pressure sensors and current meters that are fixed on pipes jetted into the sandy bottom [1] or instruments that are mounted on moving platforms such as drifters [2]. However, the nearshore is difficult to study comprehensively using only *in situ* instrumentation because a large number of instruments are required to adequately sample the scales associated with nearshore circulation, typically on the order of $10^3 - 10^4$ m. The instruments present a hazard to recreational swimmers, surfers, or boaters and are difficult to install and maintain in the harsh nearshore environment for a given length of time. Recently, remote sensing technology has been applied to studies of nearshore processes. Remote sensors are less invasive, are generally easier to deploy and maintain, and offer wider areal coverage than typical arrays of *in situ* instruments. However, because the remote measurements are indirectly related to the quantity of interest, field verification is required to establish the validity of the measurements and to understand their limitations.

Optical video-based remote sensing is perhaps the most common form of remote sensing used by the nearshore science community (e.g., [3] and [4]). Video measurements produced by so-called "time-stacking" techniques [5] have enabled estimation of quantities such as wave phase speed (celerity), wave period and direction [6], [7], and longshore surface currents [8]. Video data are also used to describe coastal morphology in terms of sandbar migration [9]–[11] and subaerial beach profiles [12]. More recently, video data have been used to estimate subtidal morphology using wave phase velocity [7], [13] and wave energy dissipation from time-averaged video images [14]. Techniques such as particle imaging velocimetry (PIV), borrowed from the fluid mechanics community [15], have been used to estimate surface currents in the swash and surf zones over relatively small spatial distances ($\approx$100 m) [16].

The use of video imagery to detect surface currents relies on adequate contrast of features in its field of view. In the surf zone, foam and bubbles generated by the breaking process create contrast with the ambient water and provides a means to observe currents by quantifying the passive advection of coherent features. Additionally, video techniques require adequate lighting conditions, which limits its utility to daylight hours.

On the other hand, radar remote sensing—with a long history in oceanographic applications resulting in the operational use of satellite-based scatterometers, altimeters, and synthetic aperture radars—is not limited to daylight hours and

Manuscript received October 15, 2008; revised January 29, 2009 and February 13, 2009. First published May 26, 2009; current version published July 23, 2009. This work was supported by the Office of Naval Research (Coastal Geosciences) under Grants N00014-02-1-0239 to the University of Massachusetts and N00014-02-1-0238 to The Ohio State University.

D. Perkovic was with the Microwave Remote Sensing Laboratory, Department of Electrical and Computer Engineering, University of Massachusetts, Amherst, MA 01003 USA. She is now with the Radar Science and Engineering Department, Jet Propulsion Laboratory, Pasadena, CA 91109 USA (e-mail: Dragana.Perkovic@jpl.nasa.gov).

T. C. Lippmann is with the Center for Coastal and Ocean Mapping, University of New Hampshire, Durham, NH 03824 USA (e-mail: lippmann@ccom.unh.edu).

S. J. Frasier is with the Microwave Remote Sensing Laboratory, Department of Electrical and Computer Engineering, University of Massachusetts, Amherst, MA 01003 USA (e-mail: frasier@ecs.umass.edu).

Color versions of one or more of the figures in this paper are available online at http://ieeexplore.ieee.org.

Digital Object Identifier 10.1109/TGRS.2009.2016556

can be utilized under most atmospheric conditions typical of coastal environments. Coarse spatial resolution, infrequent sampling, and (often) interference by adjacent land areas limits spaceborne microwave measurements of the sea to large-scale oceanographic applications in regions well seaward of the surf zone. However, because radar is largely insensitive to visibility conditions in the atmosphere, it offers the possibility of making continuous observations over large spatial areas from land-based deployments. Although the spatial resolution of radar imagery is generally inferior to that of optical techniques, it has potential to generate useful data in conditions where video data are generally unavailable.

Most radar applications in nearshore studies rely on marine navigation radars that typically operate at S-band ($\approx$3 GHz) or X-band ($\approx$10 GHz) frequencies or on high-frequency (HF) radars that typically operate at a few tens of megahertz [17]–[19]. Marine radars are useful for making observations to a range of a few kilometers with spatial resolution, O(10 m), that is sufficient to resolve the dominant surface-wave motions. HF radars are used to observe near-surface currents over regions spanning several tens of kilometers with approximately kilometer-scale spatial resolution, and while proven useful for many years for larger scale coastal oceanography, their utility at smaller scale close to the shore is limited.

Young *et al.* [20] demonstrated the use of marine radar to infer wave dispersion characteristics by photographing and subsequently digitizing successive scans of surface waves on plan-position indicator displays. Advancements in processing techniques since that time have led to applications in estimating wave and current fields [21]–[23]. Bell [24] used time series of intensity images from shore-based radar to estimate bathymetry by observing changes in the phase velocity of dominant waves. Frasier *et al.* [25] and Moller *et al.* [26] used surface Doppler signatures coupled with wavenumber-frequency wave spectra to estimate surface and subsurface current profiles. In some instances, the measurements of near-surface currents using HF radar have been taken as the true measurement of ocean surface current [18], [27] and have been taken as ground truth compared to other radar measurements of surface currents, such as those made with INSAR [28].

The focus of this paper is on comparison of radar- and video-based measurements of longshore currents obtained in the surf zone of a natural beach over a 1-km stretch of coastline. Previous observations of surface velocities obtained with Doppler radar were compared with coincident video-based observations focused on bores propagating onshore through the surf zone [29] and to subsurface *in situ* cross-shore current measurements [30]. These studies restricted the analysis to cross-shore motions within about 125 m of the radar sensor location and showed that, although radar-derived surface currents were coherent with surface video and subsurface *in situ* measurements, mean values were offset typically 0.5–1.0 m/s and, in the case of subsurface flows, were in the opposite direction (with the latter result being attributed to typical vertical structure found ubiquitously in cross-shore flows on natural beaches).

In this paper, we compare mean alongshore surface currents estimated from a single Doppler radar with an array of video PIV-based observations spanning the surf zone (approximately 200–250 m wide) and over alongshore distance up to 1.1 km from the sensor locations. Velocities estimated from the radar are along the radial beam that is oriented approximately alongshore over the extent of the investigated region of coastline. The video PIV methods allow observations of vector velocities (i.e., in both the cross-shore and alongshore directions); in the analysis herein, video-derived velocities are rotated to align with the radar radial directions and compared directly. We find that radar- and video-estimated alongshore surface currents are highly correlated both spatially and temporally. Given the differences in the scattering and imaging mechanisms, upon which the two methods rely, it is most likely that both methods are capturing the true surface flow.

This paper is organized as follows. Section II describes the field experiment, giving the layout of the instruments used in this paper. Section III outlines the theory behind radar and video imaging techniques in the surf zone and methods used to extract surface velocities from both measurements. The comparisons of surface velocity measurements are given in Section IV. Discussion and summary of results are presented in Sections V and VI, respectively.

II. Nearshore Canyon Experiment

The measurements used in this paper were obtained as part of the Nearshore Canyon Experiment (NCEX), conducted in 2003 over the months of October and November, at Black's Beach just north of La Jolla, CA. NCEX was aimed at understanding the influence of complex offshore bathymetry, such as that of the La Jolla and Scripps submarine canyons shown in Fig. 1, on wave transformation and nearshore circulation and the evolution of nearshore bathymetry. The figure shows the location of the video and radar mounted 73 m above sea level atop the NOAA Southwest Fishery Science Center building at the Scripps Institution of Oceanography (SIO). Also shown is the location of the SIO pier and contours of the bathymetry (dashed lines) and subaerial topography (solid lines). The study region of interest in this paper is located to the north of the video and radar location within about 400 m of the shore between alongshore coordinates of 500 and 1700 m. The coordinate system is local in northings and eastings translated to an arbitrary origin located near the third piling of the SIO pier. Fig. 2 shows a view of the area of interest along the coast overlooking Black's Beach from the position of the radar and video camera.

The Microwave Remote Sensing Laboratory at the University of Massachusetts (UMass) deployed a specially modified marine radar (Fig. 2) [31] at the location shown in Fig. 1. The radars were based on Raytheon Pathfinder ST/MK2 high-seas navigation radars employing 25-kW peak-power magnetron transmitters producing a 100-ns pulse every 400 μs, resulting in a range resolution of approximately 15 m over the scanned area. The antenna rotated at 40 r/min, giving a revisit time of 1.5 s. Modifications to the radars included the following: 1) changing antenna polarization (from horizontal to vertical) to improve the sensitivity to the sea surface and 2) enabling Doppler velocity measurements by replacing the receiver's stable local oscillator and data acquisition system and by recording the transmitted pulse.

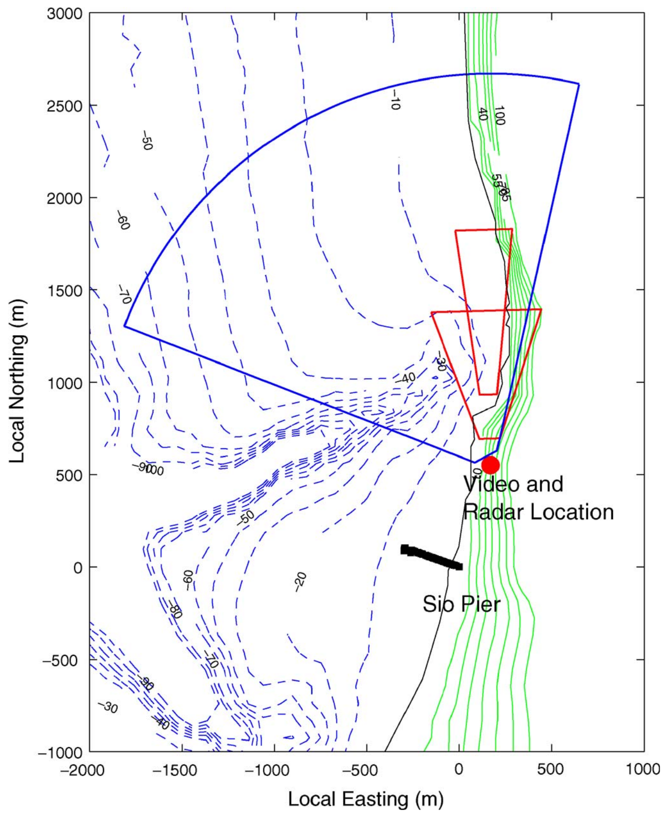

Fig. 1. Elevation contours (dashed lines: below sea level at 10-m intervals; solid lines: above sea level at 15-m intervals) showing the complex nearshore bathymetry at the NCEX field site. Coordinates are in local northing and easting relative to the SIO pier. Also shown is the location of the two video cameras and the radar atop the NOAA building.

Fig. 2. View overlooking the NCEX field site from the roof of the NOAA building with the University of Massachusetts' X-band Doppler radar in the foreground. The video cameras and RF transmitters are just out of view to the left about 2 m from the radar location.

Two Sony DC10 2-3 in analog video cameras were mounted on the NOAA building within about 2 m of the radar (Fig. 2; cameras not shown). Video images were transmitted over an RF link to a receiving station at the end of the SIO pier, approximately 1 km to the south, and digitized at 3 Hz using ATI TV-Wonder image capture boards in host personal computers running the SuSE 8.1 Linux operating system. They were time synchronized to GPS using a Horita master time code generator. Backup analog images were recorded on time-lapse video tapes at 3.75 Hz. Video images were collected during daylight hours spanning dawn to dusk. Image-to-ground-coordinate transfor-

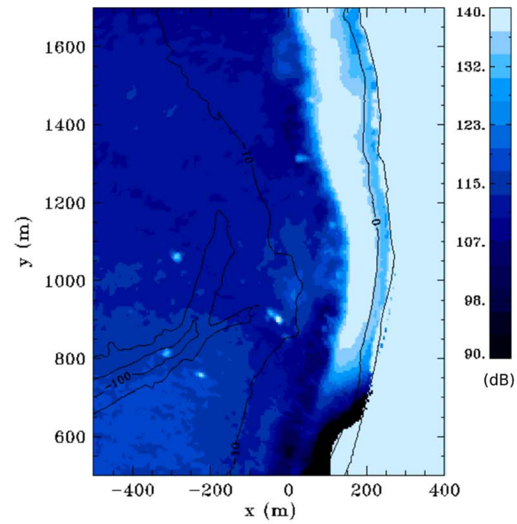

(a)

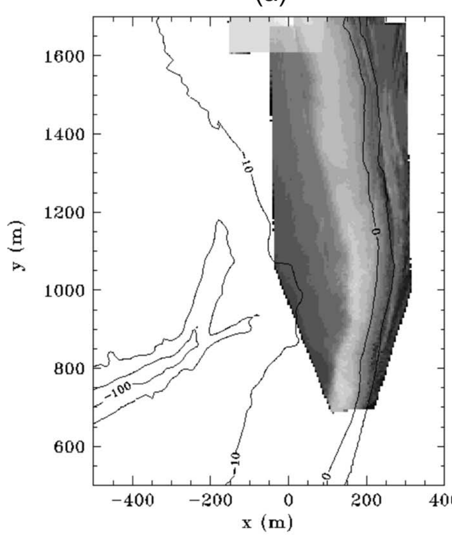

(b)

Fig. 3. Data from October 31, 2003, at 1000-h PST. Depth contours are shown in meters relative to MSL. Offshore is to the left, and the shoreline is between the 0- and 1-m contour lines. (a) Nine-minute time average of range-corrected radar echo (proportional to NRCS) indicating strong echo from the surf zone. Point echoes offshore are due to buoys deployed around the Scripps canyon. (b) Nine-minute merged video intensity from video cameras also showing surf zone extent.

mation, as well as lens distortion corrections, was done using standard methods [32]. The ground coverage of the overlapping video used in this paper is shown in Fig. 3(b), with a 9-min time-averaged mosaic of the overlapping camera views.

In this paper, we will focus on data obtained during daylight hours on October 31, 2003. On this day at 1000-h PST, the offshore root-mean-square (rms) wave height was 1.31 m, the spectral peak wave period was 7.14 s, and the dominant wave direction was 282° from the north, approximately 12° clockwise from shore normal. The wave conditions were obtained from a CDIP directional wave buoy located in 27-m water depth at location 779 m alongshore and −233-m cross-shore distance. Two other CDIP buoys located just off Black's Beach in 100- and 20-m depths showed similar conditions indicating a near-homogeneous offshore wave field. Wave conditions in the surf were modified by wave–bottom interactions over the submarine canyons that produced alongshore variations in wave height and angle at the break point. This offshore refraction produces the complex surface flow observed over the study area.

III. Theory of Measurement

A. Radar

Fig. 3(a) shows a 9-min time-averaged image of radar backscatter over the experiment area. Bright areas indicate regions of strong backscatter, while dark areas indicate regions of little or no backscatter. The backscattered power received by the microwave radar from an area extensive target is described by the normalized radar cross section (NRCS). For moderate incidence angles (between 20° and 70°), the NRCS is typically dominated by the resonant interaction of incident electromagnetic waves with surface water waves. At microwave frequencies, this Bragg-resonant scattering typically comes from wind-driven capillary or capillary–gravity waves [33].

Bragg scattering theory states that the NRCS is proportional to the surface displacement spectrum evaluated at the Bragg-resonant wavelength, $\Lambda_B = (\lambda/\sin(\theta_0))$, where λ is the radar wavelength and θ_0 is the local angle of incidence. In the case of a 10-GHz radar at near-grazing incidence, the Bragg wavelength is approximately 1.5 cm, representing coincidentally the surface waves of minimum phase velocity. Larger scale gravity wave orbital velocities are observable through their modulation of the local slope and through hydrodynamic modulation of capillary waves [34]. To capture these larger scale effects, composite surface models are often sufficient to explain most of the features of the sea surface backscatter [35].

Bragg scattering requires the surface to be only "slightly rough," meaning that surface displacement and surface slopes are small compared to the wavelength of the microwave radiation. The Bragg/composite surface theory does not, however, fully explain scattering within the surf zone where wave breaking is prevalent and the sea surface is often covered by foam, and the small-scale roughness exceeds the conditions of the slightly rough surface. Radar backscatter is significant in the surf zone, even in the absence of wind [30], since most of the roughness is mechanically generated by breaking waves (rather than solely wind generated).

Radar scattering from breaking waves is often described by the colloquial term "sea spikes" and is a significant contributor to the microwave scattering at low grazing angles. The properties of radar sea spikes due to deep-water breaking (whitecaps) differ from the surf zone (curling breakers and bores). Although they remain poorly understood, sea spikes are typically characterized by large impulsive NRCS values and large Doppler velocities, with magnitude being not inconsistent with that of typical breaking wave phase velocities. Early studies associated sea spikes to wave breaking events by comparison with video data [36]. Later studies found that sea spikes are not always associated with visible breaking waves when observed at low grazing angles and concluded that sea-spike events may arise from scattering by steep-wave features, microbreakers, or plumes [37]–[40]. Additional field and laboratory studies of low-grazing-angle microwave and video scattering have observed broad Doppler spectra for breaking waves in the surf and swash zones [29], [41]–[44] and show significant backscatter for steepening, breaking, as well as broken bores.

B. Doppler Radar Signature in the Surf Zone

Fig. 4(a) shows a 9-min time-averaged image of Doppler velocities obtained from the radar at NCEX. The mean Doppler shift is calculated by means of a very efficient covariance or "pulse pair" technique. The covariance calculation estimates the first moment of the Doppler spectrum using the phase difference of echoes from successive pulses [45]. The velocity estimate is given by

$$v(t) = -\frac{\lambda}{2\pi}\frac{\phi(t)}{2\tau\sin\theta_i} \tag{1}$$

where λ is the radar wavelength, θ_i is the local angle of incidence between the incident radar pulse and the ocean surface, and $\phi(t)$ is the angle of the covariance of echoes from successive pulses separated by the pulse interval τ

$$\phi(t) = \arg\left(\langle E_i E^*(t-\tau)\rangle\right). \tag{2}$$

This phase difference is proportional to the radial displacement of a scatterer over the period τ given in seconds.

The apparent velocity determined from the Doppler centroid includes contributions from Bragg-resonant wave phase velocities (when Bragg scattering dominates), the line-of-sight component of the surface current, and the line-of-sight component of the orbital velocity of larger scale surface waves. Hence, to extract a true surface current measurement from a Doppler velocity, the influences of Bragg-resonant phase velocity and of wave orbital velocities should be removed. Determining the first requires knowledge of the directional spectrum of capillary waves (or, at least, the relative wind direction if the capillary waves are wind driven [26]). Temporal variations in the Doppler velocity are dominated by the wave orbital velocity. In the case of well-resolved waves, such as the one in this paper, averaging sufficiently over time (i.e., over many wave periods) will largely mitigate the effects of orbital velocities, although it will not completely eliminate them. For the purpose of this paper, it is sufficient to note that the region observed by the radar is dominated by mechanically induced, rather than wind-induced, roughness, with Doppler velocities associated with roughness elements being advected laterally by surface currents. Furthermore, scatterings from bores and from regions of "white water" likely violate the assumptions of a slightly rough surface. Thus, contributors to Doppler velocity, such as the phase velocity of Bragg-resonant waves, may not apply. We discuss this issue further in Section V.

C. Video Signature in the Surf Zone

The contrast in video images comes from changes in brightness due to wave breaking and reflection of incident light off the sea surface. The sharp contrast between specular scattering of light from foam and bubbles generated by breaking waves and bores and the nonbreaking (darker) water provides the primary signal used to infer nearshore processes. For example,

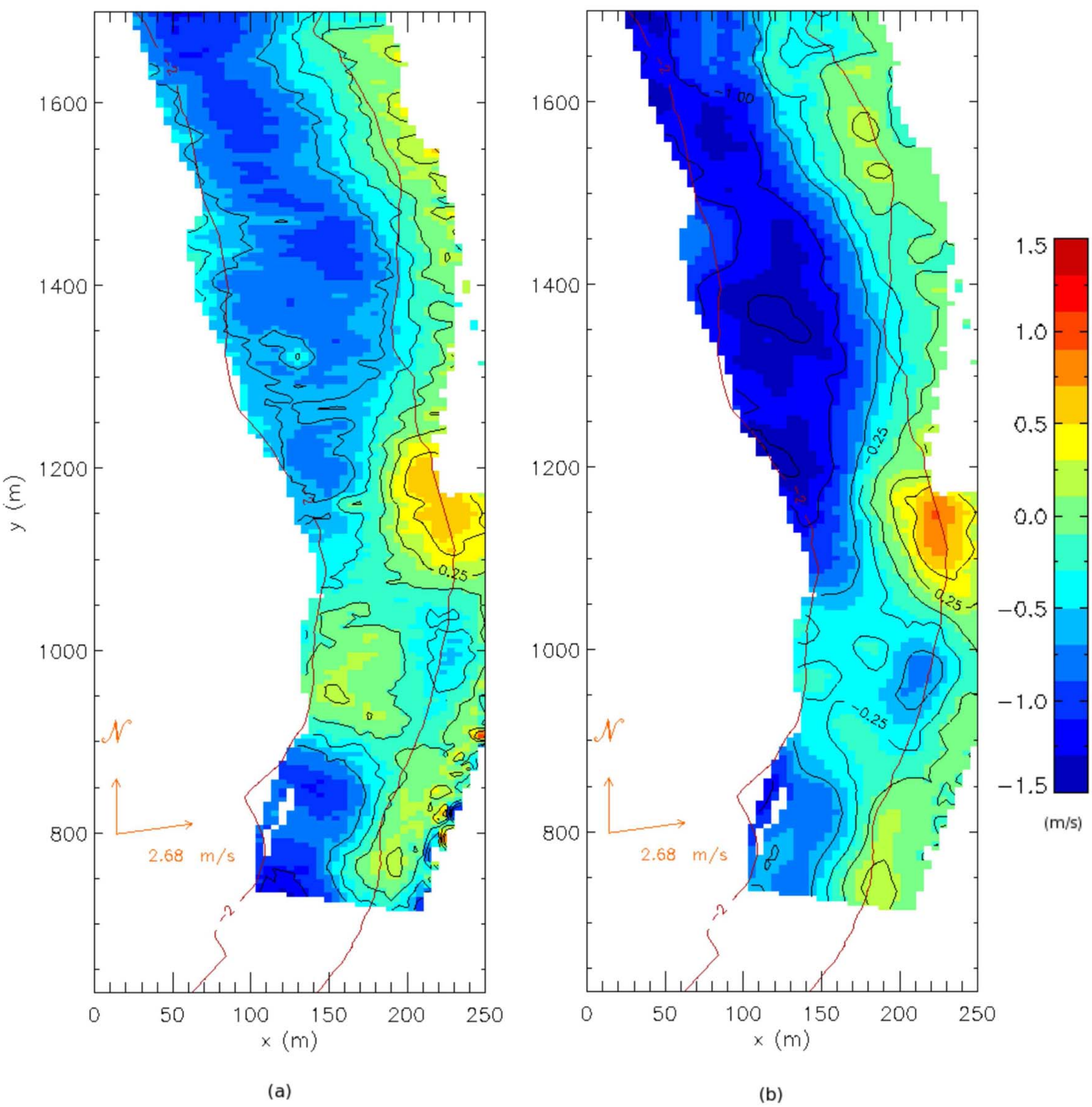

Fig. 4. Nine-minute averaged radial (approximately longshore) surface velocity starting at 1000-h PST, October 31, 2003, along Black's Beach, La Jolla, CA. (a) Radar Doppler radial velocity. (b) Video PIV radial velocity. Velocity magnitudes are shown by the color bar on the right-hand side. Wind direction and magnitudes are shown with the direction arrows relative to true north in the bottom left.

time-averaging video images over (typically) about 9 min produces a smooth pattern of average wave-breaking distribution qualitatively related to patterns of wave dissipation [3], [14]. Fig. 3(b) shows a time-averaged video intensity composite image combining the views from two colocated video cameras. The time-averaged imagery from each camera view is extracted separately over the same period and then overlaid on top of one another to produce a mosaic. The image intensities are recomputed in the overlapping region by a weighted average of the overlapping pixels from all cameras that cover the region. The weight is based on the exponential decay across the image, left and right about the center line of the camera view, and a hyperbolic decay away from the image based on the distance from the camera center. The weights are then normalized so that the average in the overlapping region is equal to one. The bright area in the image is produced by wave breaking in the surf zone. The darker areas are regions where there is no significant breaking. For our purposes, only the highly dynamic region of the surf zone produces the necessary contrast to detect surface currents.

Surface currents are estimated using particle image velocimetry (PIV) techniques, similar to previous methods [16]. PIV methods are based on the assumption that advection of surface features optically visible in video frames (for surf zone applications, most commonly bubbles and foam created by actively breaking waves and bores) is determined by comparative analysis of two successive frames. The main assumption is that the features, particles, or textural patterns are passively advected by the flow. An area of interest is selected within a pair of rectified (orthonormal) video images, for example, a region corresponding to the surf zone and extending down the coast a given distance that is dependent on the image resolution. A square search window, I, of defined dimensions is selected from the first image and correlated with many spatially lagged search windows with the same dimensions, S, obtained from the second image separated by a small time Δt. In our case, we do not compute the 2-D cross-correlation function since it has poor properties compared to the least squares error approach because the scales of variation are often larger than the integration window I [46]. Typically, a minimum error function is used in PIV techniques, including those used in surf zone applications [16], [29]. In our methods, we use the motion estimation processor (MEP) defined by [47]

$$\Phi_{i,j} = 1 - \frac{\sum_1^a \sum_1^b (|I - S|)}{2\sum_1^a \sum_1^b (I)} \tag{3}$$

where i and j are the spatial indices and a and b are the pixel dimensions of I. A 2-D Gaussian distribution is fit to the peak of the MEP matrix to estimate displacements $(\Delta x, \Delta y)$ with subpixel resolution [48]. Cross-shore and alongshore velocity magnitudes are calculated as u and v, respectively, by

$$u = \frac{\Delta x}{\Delta t} \qquad v = \frac{\Delta y}{\Delta t}. \tag{4}$$

Instantaneous velocities obtained with PIV are inherently noisy and must be filtered to remove spurious vectors. Typically, velocity vectors are compared with neighboring vectors and then replaced if they exceed a threshold in either magnitude or direction (e.g., [15], [16], and [48]). For our methods, we smooth the data with scales $2I$ using optimal interpolation [49]. Results presented herein were computed with I equal to 8×8 m, pixel resolution of 0.25 m/pixel, and $\Delta t = 1.0$ s.

A fundamental assumption when quantifying video data with nearshore applications is that the elevation of the sea surface is known and uniform at the same elevation. This is, of course, not true as there are surface waves that modulate the surface and a mean slope owing to setup processes (the superelevation of the water level driven by radiation stress gradients in the surf zone). In most applications, the relative difference between the height of the waves and the elevation of the camera makes the errors associated with uncertain image-to-ground transformation insignificant, except perhaps in the situation where waves in the far field block the view of the sea surface behind wave crests. However, in our PIV application, we wish to detect motion of passively advected features. If we assume a constant sea surface elevation in the rectification of all images, then any vertical motion not accounted for will move the apparent position of surface features horizontally. This is most easily visualized by assuming a sea surface without waves, but that is moving vertically up and down as a plane. Although there is no horizontal velocity, the video frames detect an apparent velocity that is dependent on both the rate of vertical motion and the camera look angle. For camera views looking directly downward, there is no apparent change in horizontal motion at the nadir pixels. For oblique look angles, however, there is an apparent velocity that is induced in the PIV estimates. The magnitude of this change depends on the look angle relative to the sea surface slopes. As the front and rear faces of the waves are of opposite signs, there is also a mean bias that is introduced. This bias is zero for downward-looking camera views, approaches the wave phase speed as the look angle moves toward the horizon, and becomes infinite when the wave crest shelters the rear-facing slope of the wave from the camera view. Corrections for bias velocities to PIV-estimated surface currents within the surf zone can be made, provided that the bathymetry is known and wave saturation is assumed. Bias velocity corrections were made to the NCEX databased on the formula derived in the Appendix. Because the wave field was propagating approximately normal to the camera look direction, magnitudes of bias velocities were small (< 0.10 m/s) over most of the study area; a notable exception is in the far field at the outer reaches of the surf zone where the resolution is poor, look angles are more grazing, and bias velocities are correspondingly higher (approaching 1 m/s). Fig. 4(b) shows a 9-min time-averaged alongshore surface velocity (oriented along the radial component of the radar beams) derived from video data using PIV techniques with bias corrections.

It should be noted that bias velocities can typically be neglected for purely along-crest look angles (for example, looking alongshore down the coast) or at close range from the camera (within 100–200 m of the camera location for typically high-oblique look angles). These bias velocities have not been considered in previous work, but because of the relatively close ranges considered in those studies, they were probably not a large concern in relation to other sources of error.

IV. Results

Fig. 4 shows the color contour images of 9-min time-averaged radar and PIV radial velocities over the region corresponding to the field of view of the video cameras at 1000-h PST on October 31, 2003, during NCEX. The velocity scale shown in Fig. 4 ranges ± 1.5 m/s and is colored the same in the radar and PIV surface velocity maps. As the radar only measures the radial velocity component from its location, the PIV vector velocity estimates were projected onto the radar's radial direction for comparison.

A right-hand Cartesian coordinate system was used with positive y-axis pointing north and positive x-axis pointing east, with origin being located near SIO pier piling number 3 (as in Fig. 1). The PIV velocity data were smoothed onto a 5-m cross-shore (x-direction) by 20-m alongshore (y-direction) grid. The radar data had an approximate 15-m radial range resolution (approximately alongshore) and continually decreasing resolution in the cross-shore due to beam spreading with increasing range distance.

The location of the radar and video cameras (Fig. 1) is such that the radial velocity is very nearly alongshore at NCEX; thus, the velocities shown are essentially longshore currents. Both radar and video data were linearly interpolated onto a common grid with 5 m $\times$ 5 m spacing for comparison in Fig. 4. The white region in Fig. 4 is outside the video field of view, on dry beach, or represents the missing data in both images. Good agreement between radar and PIV is clearly evident. Similarities of spatially varying longshore current features are clearly visible. At about 1100-m distance alongshore the surface, the longshore current reverses direction with southerly flow near the shore (toward the radar; blue color) and northerly flow (away from the radar; red color). This feature is suggestive of a strong

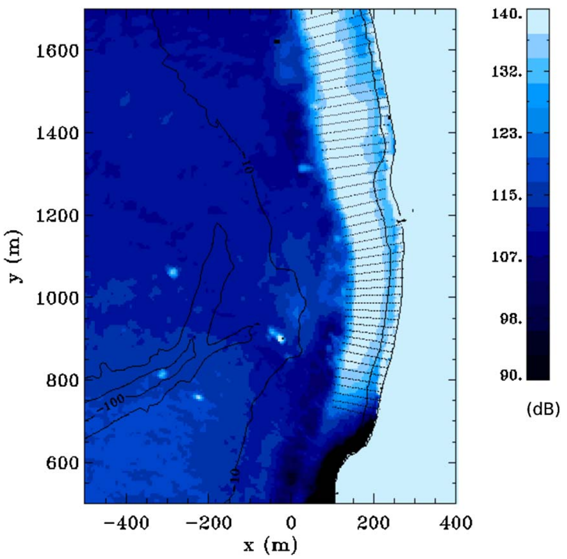

Fig. 5. As in Fig. 3(a), with video PIV velocity transect locations being overlaid. Successful PIV retrievals are limited to the surf zone.

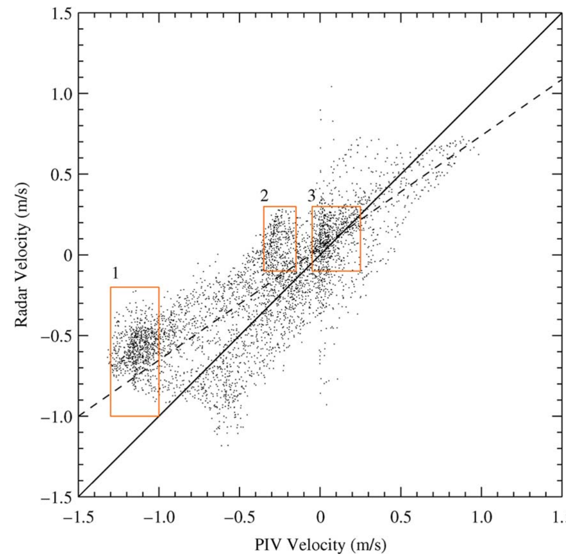

Fig. 6. Scatter plot of all available radar Doppler velocities versus corresponding PIV radial velocities. The correlation coefficient squared is calculated at 0.65. Clusters of dense points are identified in boxes 1, 2, and 3 described in text and in Fig. 7. These clusters are primarily responsible for the (dashed line) slope (0.60) of the best fit through the data.

seaward flowing current and eddylike structure at that location. In general, the radar and PIV surface velocity maps agree quite well over the 1-km alongshore region examined.

This particular period is of particular interest because the wind conditions at the time of collection measured at the end of the SIO pier (2.7 m/s from south to southwest) were below the threshold needed for significant (Bragg) scattering outside the surf zone. This is consistent with low radar signal levels beyond the surf zone, as indicated by the time-averaged backscatter intensities [Fig. 3(a)]. Similarly, the mosaicked video image [Fig. 3(b)] shows a distinct lack of breaking (whitecapping) seaward of the surf zone.

Fig. 5 shows the cross-shore transects where video PIV velocity estimates were computed. These are overlaid on top of the averaged backscatter radar image. We find that the extent of the transects for which reasonable PIV estimates were obtained corresponds closely to the enhanced backscatter of the surf zone. This result is expected as the video contrast (hence signal strength) decays rapidly seaward of the surf, and is a useful check of the cross-shore alignment of the two data sources.

Fig. 6 shows a scatter plot of radar radial velocities versus PIV radially aligned velocities over all transects shown in Fig. 5. The plot shows a positive correlation (value $r^2 = 0.65$) between video and radar data. When all points are included, the dotted line is the best fit to scatter data with a slope of 0.60, while the solid line represents the ideal (1 : 1) fit.

We note three somewhat distinct clusters of points appearing in the scatter plot, labeled by boxes 1, 2, and 3. By examining the points that lie within these boxes, we find that these clusters of points correspond to particular spatial locations shown in Fig. 7(a), where we have overlaid the points on top of the Doppler radar velocity image. White squares indicate the positions of points in the scatter plot that belong to box 1, black asterisks represent the points within box 2, and black squares are the points collected in box 3.

Approximately 80% of the points within boxes 1 and 2 are found along a contour line following the outermost edge of the surf zone. This is the area where the waves steepen sharply and initially break and are viewed obliquely by the radar with a slightly northward component to their phase velocity. The remaining 20% of points in boxes 1 and 2 occur along a contour where the alongshore velocity changes sign from up- to downcoast directions. Most of the points contained in box 3 are found along a contour line following the inner edge of the swash zone.

We can eliminate the biasing locations close to the breaker and swash edges by extracting only those data between the swash zone and seaward edge of the breaker line (i.e., the surf zone), represented by the dashed contours in Fig. 7(b). The locations of surf zone edge and shoreline were estimated from the time stacks of video data. A scatter plot of only these surf zone data is shown in Fig. 8. The best fit line for the velocities within the surf zone between the dashed lines has a slope of 1.02, which is very close to the ideal 1 : 1 slope fit. The rms difference in velocity values for the surf zone is 0.18 m/s, while the correlation coefficient squared is 0.79. Thus, within the surf zone, the longshore velocities observed by both techniques are quantitatively consistent and with small (2%) bias.

For the data examined here, the good agreement between radar Doppler velocities and PIV radial velocities within the surf zone suggests that no Bragg-resonant phase velocity correction is required to account for wind effects, as would normally be the case in open water beyond the surf. One possible reason is that the dominant scatterers are broken waves and bores that are largely traveling across the radar beam, inducing little radial velocity component other than lateral advection by the longshore current. These roughness elements, with displacements of a few to several centimeters, are better characterized as a “very rough” surface and do not fit the Bragg scattering model. Between bores, it may be the case that Bragg scattering occurs, however, since the source of surface roughness is largely mechanical, and the directional spreading of Bragg-resonant waves may be expected to be broad,

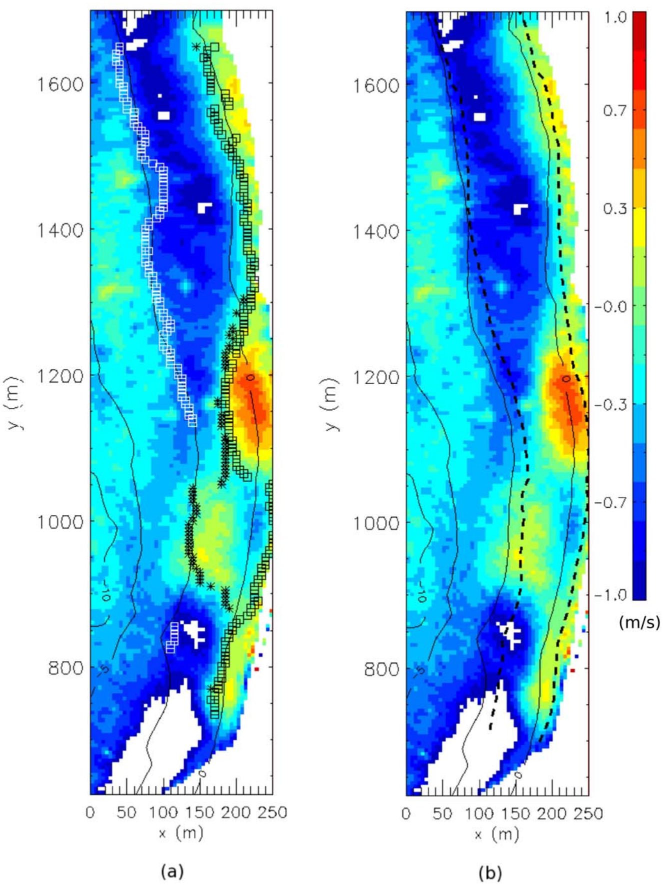

Fig. 7. Radar Doppler velocity image overlaid with (a) locations of points in clusters 1, 2, and 3 from scatter plot in Fig. 6 and (b) (dashed) surf zone width and shoreline locations determined from video intensity time stacks.

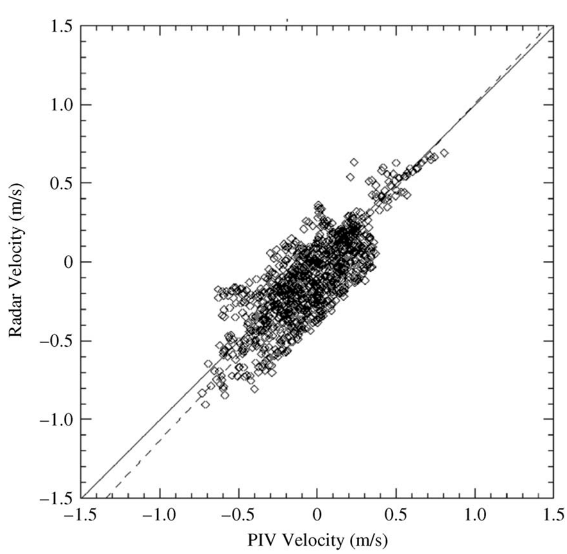

Fig. 8. Scatter plot of radar Doppler velocities versus corresponding PIV radial velocities over the surf zone alone, between the dashed contours in Fig. 7(b). The correlation coefficient squared is 0.79.

such that the radar encounters waves traveling both toward and away from it, thereby inducing a net component of near zero, as described by Moller *et al.* [26] and Thompson and Jensen [50].

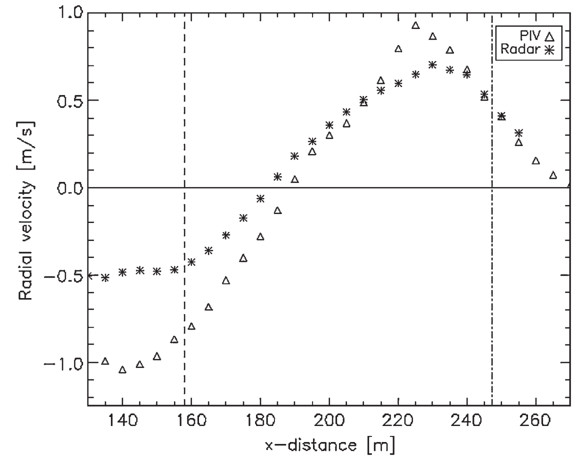

Fig. 9. Cross-shore transect of Doppler and PIV velocities at 1140 m alongshore. Velocity estimates are 9-min averages. The dashed line on the left marks the approximate location of the initial breaker zone, and the dot–dashed line on the right marks the approximate edge of the swash zone.

In nearshore process field studies, the cross-shore profiles of the near-bottom alongshore currents have been observed and confirmed with numerous models, leading to the primary understanding of dynamics in the surf (e.g., [1], [51], [52], and many others). Typically, current profiles are observed at a single or few sparsely (O(10–20 m) spacing) instrumented cross-shore transects [53]. The nature of remote sensing instruments examined herein allows for dense observation of mean longshore currents and horizontal circulation patterns, revealing the strong spatial variability missed with more sparsely located instrumentation (for example, the eddylike current structures seen in Fig. 4). Fig. 9 shows a comparison of the longshore current profile along a single transect at the alongshore distance of 1140 m. Both PIV and radar velocities show the same form, going from negative (southerly) flow at distances farther offshore to positive (northerly) flow closer to the shore. The radar velocities between 130- and 170-m cross-shore distances are approximately constant at −0.5 m/s, whereas PIV velocities range smoothly from −0.9 m/s at 120 m to −0.5 m/s at 170 m, peaking at about −1.0 m/s at a cross-shore location of 140 m. Also, PIV velocities peak at a higher northerly flow (1.0 m/s) at 230-m cross-shore distance, and between 240- and 280-m cross-shore distances, the radar and PIV velocities track each other closely. Video-derived estimates of the mean surf zone width on this transect indicate that the seaward edge of the surf zone is located at approximately 154-m cross-shore distance and labeled by the dashed line in Fig. 9, placing most of the divergent velocity points near the seaward breaker line. The approximate position of the shoreline (estimated from the intersection of mean sea level with the foreshore beach profile) is shown with the dot–dashed line in Fig. 9.

The spatial variation spanning about 1 km alongshore in longshore current profiles is shown in Fig. 10. The inner breaker zone edge and the outer swash zone edge are shown as dashed and dot–dashed lines on the left- and right-hand sides, respectively. In general, the radar and video mean surface longshore current profiles track each other reasonably well. In particular, flows are always recorded in the same direction (up

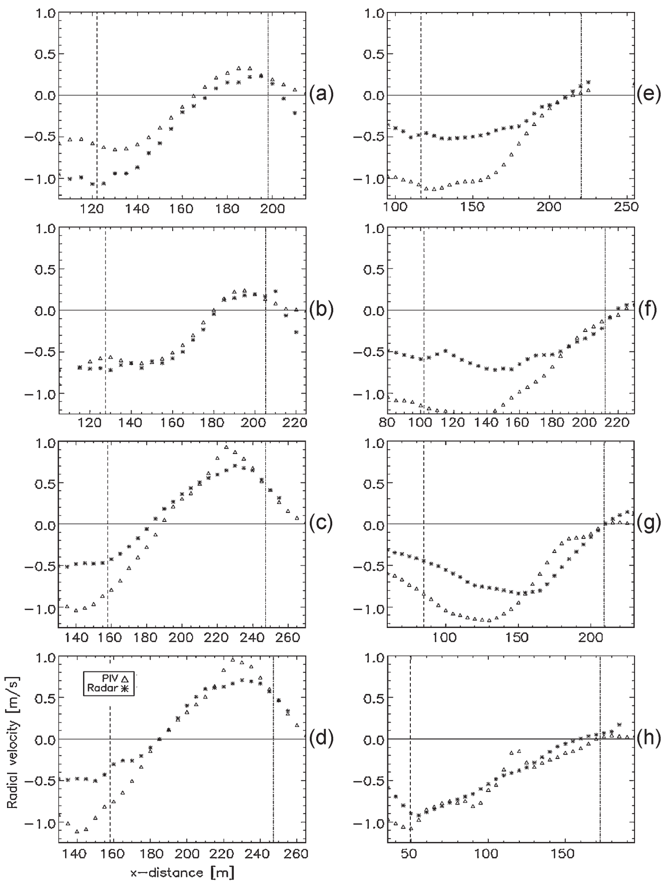

Fig. 10. As in Fig. 9 at several alongshore locations: (a) $y = 750$ m, (b) $y =$ 800 m, (c) $y = 1140$ m, (d) $y = 1150$ m, (e) $y = 1275$ m, (f) $y = 1350$ m, (g) $y = 1450$ m, and (h) $y = 1650$ m.

or down coast), even in situations where the longshore current reverses direction along a cross-shore transect, and the point where zero-crossing occurs is, in general, the same between sensors. However, at some locations, the measurements deviate in magnitude by as much as 0.5 m/s, with the radar currents generally about one-half that of the video. Part of the spatial variation is due to inaccuracies in the video image-to-ground transformation, particularly for the estimate of tilt angle in the far field where the resolution degrades and the uncertainties in the measured orientation increase. Small errors in ground coordinates can result in significant mismatch if the spatial variability in mean flow is high, such as the case for the data examined on October 31, 2003. Coregistration is also complicated by degrading spatial resolution owing to finite radar beamwidths. These errors will be discussed further in the next section.

The temporal variation of short 3-min averages of currents derived from each sensor is examined with time series of mean velocities at 800-m alongshore and 175 m cross-shore coordinates and is shown in Fig. 11. The total duration of the time series is 6 h starting at 0600-h PST on October 31, 2003, and ending at 1143-h PST. The correlation coefficient squared is 0.78, and the rms difference is 0.05 m/s. The time series each follow one another closely, showing temporal variations on the order of 0.5 m/s over 10–20-min intervals, as well as a general trend to weaker mean flows toward the end of the run. A short-duration temporal lag (persisting for about 1 h) between PIV and radar measurements of 3–6 min is observed toward the end of the 6-h time series.

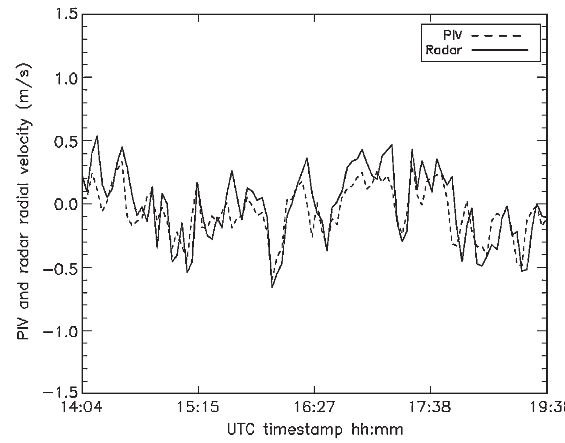

Fig. 11. Six-hour time series of (solid line) radar and (dashed line) video velocity estimates beginning at 0600-h PST on October 31, 2003, and located at 800-m alongshore and 175-m cross-shore distances. The velocity estimates are 3-min averages.

V. DISCUSSION

In the previous section, we described the comparison between video- and radar-derived mean longshore surface velocities across the surf zone over a 1.1-km distance up the coast. The two techniques obtain very similar estimates of mean longshore currents within the surf zone, while there are differences in measurements at the seaward (breaker line) and shoreward (swash) edges of the surf zone (Figs. 6, 9, and 10). These differences can amount to as much as 0.6 m/s, significantly higher than can be attributed to either wind-induced or Bragg-resonant phase velocities detected in the radar signal. A possible explanation is that radar- and/or video-derived longshore velocities in the breaker zone are contaminated by steep breaking waves that, at these locations, are viewed obliquely.

Near the breaker line, the rms velocity difference between radar and video mean longshore surface currents is 0.33 m/s, while in the surf zone, this difference reduces to 0.18 m/s. Also, in this region, PIV-derived velocities are generally larger than the estimates from radar. As the waves on October 31, 2003, approach the shore from a northerly direction (driving the strong alongshore current to the south; observed in the figures), we expect some contamination at the breaker line (as reported by Puleo [29]). Although steps to eliminate the high velocities are made in the filtering procedures, it is likely that some bias in PIV estimates at the edge of the surf zone exists. This effect is apparently much reduced in the radar estimates. Similarly, the peak incident-wave direction at the offshore break point indicates that the waves were not perpendicular to the radar and video look angles, and so, their apparent alongshore phase speed might contribute to measurements of surface velocity. Waves with 7.14-s period have phase velocities of O(5–6 m/s) at the edge of the surf zone in about 3-m water depth. The maximum radial component of this velocity along the breaker zone (considering both 12° wave direction and the look direction of the radar beam) is estimated at approximately -2.4 m/s. We do not see evidence of velocities of this magnitude in the radar data, except in the video data, suggesting that contamination by obliquely propagating waves is likely evident in the radially aligned PIV current estimates, particularly near the breaker line where the wave angle is greatest.

With respect to the influence of wind effects impacting Doppler measurements, we chose to not attempt any correction for wind (i.e., Bragg-resonant phase velocity correction). The reason for this is twofold. First, the dominant source of microwave backscatter observed within the surf zone, namely, the bores, is non-Bragg scattering elements. Second, attempting a wind correction here is problematic due to the proximity and influence of large cliffs near the shoreline. Offshore wind estimates, either from buoys or the SIO pier, may not be indicative of the wind at the location(s) probed by the radar. Winds were low in any case. The impact of wind-generated roughness in the surf zone may be expected to be different at less sheltered beaches under stronger wind forcing.

In images of radar surface Doppler velocities, we note that the exposed beach and cliffs often return nonzero Doppler velocities, even though they are stationary targets. The nonzero Doppler velocities are distributed somewhat randomly in space but do not change with time. We attribute this observation to the mechanical scanning of the antenna viewing the oblique surface during the finite integration time used to estimate velocities. Although the surface is stationary, the centroid of scattering "moves" radially as the antenna's beam passes over it. This effect is not present in the time-varying water surface that is, on average, flat. Thus, the scatter in velocities seen by the radar at the shoreline is likely influenced by this scanning effect.

At the larger observation distances, the differences between video and radar velocity estimates generally increase. As range increases, both radar and video spatial resolutions degrade, resulting in larger averaging areas or footprints. The increase in footprint sizes reflects in differences in spatial location between the two systems. In regions of high spatial variation in the mean flow field, this spatial location error would account for some of the differences observed at distances greater than about 600 m from the camera. In addition, small errors in orientation parameters used to transform video images into orthonormal reference frame lead to large spatial errors in pixel ground locations. Errors of 0.1° in tilt angle result in 24.6-m ground errors at a range of 1000 m from the camera. As this region exhibits high spatial and temporal variabilities in mean flow patterns, spatial offsets in comparison with radar can be large. This spatial error does not enter into radar estimates as distances to targets are precisely known (within the footprint of the radar pulse) from the travel time between the transmitted pulses and the received echoes.

A 2-D (spatial) lagged cross-correlation between radar and PIV velocities was computed over the entire study area, resulting in a peak correlation squared of 0.93 occurring at the alongshore shift of 30 m corresponding to the distance covered by two radar range bins and 2–45 image pixels, depending on range from the camera and radar (corresponding to 15–0.66 m/pixel, respectively). The images were divided into five sections up coast starting from 725 m alongshore distance every 150 m, and a 2-D cross-correlation was computed on each section. The maximum correlations were found to peak at different alongshore shifts, and the corresponding lag indicates a positional error as large as 15–30 m in the alongshore direction. Shifting of video data resulted in a decrease in rms difference of velocities in the surf zone from 0.18 to 0.13 m/s and an increase in correlation coefficient squared from 0.79 to 0.91.

The time lag of about 3–6 min observed for a 1-h period in the 3-min mean alongshore flows is also likely due to spatial misregistration between radar and PIV measurements in the presence of high spatial variability. As the spatial misregistration was approximately 15–30 m in the alongshore direction, the current features propagating in the alongshore direction are estimated to be moving at speeds between 0.06 and 0.12 m/s, quite possibly associated with alongshore migrating current structure that is common to most natural beaches. If we compare this range of speeds with Fig. 4 at 800-m alongshore and 175-m cross-shore distances, and assuming that the radar measures the alongshore component of the flow, we observe the same range of velocities. As a result, we believe that the observed differences between radar and video within the surf zone are dominated by errors in external image-to-ground geometrical transformations and internal intrinsic camera parameters (such as lens distortion [32]). The problem is further exaggerated by physical changes to the camera system that occurs as the temperatures of components vary during the day [54]. This evolution in geometry could lead to temporal offsets observed in the time series.

VI. Summary

This paper has presented a comparison of mean longshore surface currents measured by video PIV and Doppler radar remote sensing techniques. In general, surface currents show very good quantitative agreement as the changes in the direction of the surface currents varied alongshore over the 1.1-km range from the radar and video locations. Correlation between PIV and Doppler radar estimates shows reasonable agreement over most of the surf zone, resulting in a best fit line with the slope of close to one and rms difference of 0.18 m/s. Some 6-h time series of 3-min averages at mid surf zone positions are highly correlated ($r^2 = 0.78$) and have low rms difference (0.05 m/s), suggesting that both remote sensing techniques are reasonably and accurately measuring the mean longshore surface current. The spatial and temporal misregistrations of data sets account for much of the scatter in the data and are believed to be responsible for both apparent spatial and temporal lags observed.

Radar and video surface current measurement techniques have historically suffered from a lack of independent verification. As they both sense surface properties, it is often very difficult to compare remote observations to *in situ* measurements that are necessarily obtained at depth (usually near the bottom well below the surface). The fact that both measurements indicate very similar surface velocities within the surf zone and that both rely on very different mechanisms suggests that the true surface velocity is being captured with reasonable accuracy.

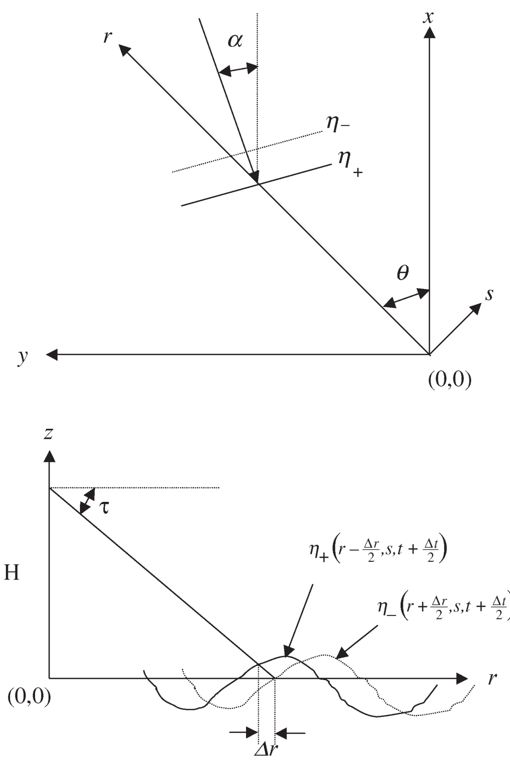

Fig. 12. (Top) Coordinate system aligned with the look direction showing rotation relative to wave angle and the Cartesian coordinates with x shore normal. (Bottom) Schematic showing the apparent horizontal displacement observed from an oblique point of view during the passage of a wave crest over a short time interval.

APPENDIX

In this section, mean (phase-averaged) corrections to estimates of surface velocities derived from video PIV analysis in the presence of a shoreward-propagating surface wave field are derived. The bias velocities are dependent on the camera view geometry relative to the wave direction.

The video camera is located at an elevation H above mean sea level and at the origin of a right-handed coordinate system, with the positive x-axis being directed shore normally and the positive y-axis being directed alongshore. The look direction of any point in the image (pixel) is defined by a rotation angle measured counterclockwise from the positive x-axis θ and a tilt angle τ measured downward from horizontal. The bias velocities will be derived in a rotated coordinate system (r, s) defined by θ (Fig. 12, top).

We consider a general wave field η composed of a sum of N discrete sinusoids with radian wavenumber vector κ_n and radian frequency σ_n, propagating toward the shore in the general $-x$ direction

$$\eta(x,y,t)=\sum_{n=1}^{N} a_n\cos(k_nx+l_ny-\sigma_nt)+b_n\sin(k_n+l_ny-\sigma_nt) \tag{5}$$

where k_n and l_n are the cross- and alongshore wavenumber components, respectively, that define the wave direction $\alpha_n=\arctan(l_n/k_n)$ of each wave component with frequency $f_n=\sigma_n/2\pi$, t is time, and the Fourier coefficients a_n and b_n describe the wave amplitude $\eta_n=(a_n^2+b_n^2)^{1/2}$ and phase $\phi_n=\arctan(b_n/a_n)$, respectively. Thus, η describes the time-varying displacement of the sea surface at any locations x and y. In PIV analysis, horizontal displacements of a surface signature are determined over a time interval Δt. If we consider the wavefield one-half time step before and after any arbitrary time, η_- and η_+, respectively, then

$$\eta_-=\sum_{n=1}^{N} a_n\cos\left(k_nx+l_ny-\sigma_n\left(t-\frac{\Delta t}{2}\right)\right) + b_n\sin\left(k_n+l_ny-\sigma_n\left(t-\frac{\Delta t}{2}\right)\right) \tag{6}$$

$$\eta_+=\sum_{n=1}^{N} a_n\cos\left(k_nx+l_ny-\sigma_n\left(t+\frac{\Delta t}{2}\right)\right) + b_n\sin\left(k_n+l_ny-\sigma_n\left(t+\frac{\Delta t}{2}\right)\right). \tag{7}$$

Video systems that observe the wave field at the look angle τ perceive the location of the wave surface at horizontally displaced positions that are dependent on their elevation relative to mean sea level (a common occurrence for 2-D imaging systems that record nonplanar processes such as surface ocean waves). This so-called layover has a time-varying distance that is dependent on the height and phase of the waves and causes an apparent, or bias, velocity in PIV analysis. The magnitudes of the bias displacements in the cross-shore and alongshore directions, Δx and Δy, respectively, are manifested in the video as apparent phase shifts, $k_n\Delta x$ and $l_n\Delta y$, shared between η_- and η_+, such that

$$\eta_-=\sum_{n=1}^{N} a_n\cos\left(k_n\left(x+\frac{\Delta x}{2}\right)+l_n\left(y+\frac{\Delta y}{2}\right)-\sigma_n\left(t-\frac{\Delta t}{2}\right)\right) + b_n\sin\left(k_n\left(x+\frac{\Delta x}{2}\right)+l_n\left(y+\frac{\Delta y}{2}\right)-\sigma_n\left(t-\frac{\Delta t}{2}\right)\right) \tag{8}$$

$$\eta_+=\sum_{n=1}^{N} a_n\cos\left(k_n\left(\frac{x-\Delta x}{2}\right)+l_n\left(y-\frac{\Delta y}{2}\right)-\sigma_n\left(t+\frac{\Delta t}{2}\right)\right) + b_n\sin\left(k_n\left(x-\frac{\Delta x}{2}\right)+l_n\left(y-\frac{\Delta y}{2}\right)-\sigma_n\left(t+\frac{\Delta t}{2}\right)\right). \tag{9}$$

Using simple geometrical considerations (Fig. 12, bottom), the apparent bias displacement along the look direction ($+r$-axis), Δr, of a surface signature over the time interval between image pairs is then given by

$$\eta_- - \eta_+ = -\Delta r\tan\tau. \tag{10}$$

Substitution of (6) and (7) into (10) gives

$$\begin{aligned}\eta_- - \eta_+ = &\sum_{n=1}^{N} 2a_n \sin(k_n x + l_n y - \sigma_n t)\\ &\times \sin\left(k_n \frac{\Delta x}{2} + l_n \frac{\Delta y}{2} - \sigma_n \frac{\Delta t}{2}\right)\\ &- 2b_n \cos(k_n x + l_n y - \sigma_n t)\\ &\times \sin\left(k_n \frac{\Delta x}{2} + l_n \frac{\Delta y}{2} - \sigma_n \frac{\Delta t}{2}\right)\\ = &- \Delta r \tan\tau. \end{aligned} \tag{11}$$

When

$$k_n \frac{\Delta x}{2} + l_n \frac{\Delta y}{2} - \sigma_n \frac{\Delta t}{2} \ll 1 \tag{12}$$

(11) can be solved for the bias velocity in the look direction

$$\frac{\Delta r}{\Delta t} = \frac{-\frac{\partial \eta}{\partial t}}{\frac{\partial \eta}{\partial x}\cos\theta + \frac{\partial \eta}{\partial y}\sin\theta - \tan\tau} \tag{13}$$

where we have used the trigonometric relations $\Delta x = \Delta r \cos\theta$ and $\Delta y = \Delta r \sin\theta$. The corresponding cross-shore $u_{\rm bias}$ and alongshore $v_{\rm bias}$ components of the bias velocity are given by

$$u_{\rm bias} = \frac{\Delta r}{\Delta t}\cos\theta \qquad v_{\rm bias} = \frac{\Delta r}{\Delta t}\sin\theta. \tag{14}$$

Equation (13) shows that the bias velocities are determined by the vertical motion of the sea surface as waves propagate past any given point, divided by the difference in the sea surface slope along the look direction of the camera and the tangent of the tilt angle relative to the horizon. When the camera view is directly overhead, $\tan\tau$ is infinite, and the bias velocities go to zero; thus, it is advantageous to have camera views that are as downward looking (hence highest camera vantage point) as possible. At some intermediate value, a critical tilt angle, $0 < \tau_c < \pi/2$, will equal the seaward slope of the wave in the look direction, in which case the bias velocities become undefined. As τ approaches τ_c, the bias velocities rapidly increase. When $\tau > \tau_c$, the sea surface is obscured by the wave crest, and in the limit, as τ approaches the horizon ($\tau = 0$), the PIV estimates are biased toward the phase speed c_n of the individual wave components, such that $(u_{\rm bias}, v_{\rm bias}) = c_n/\cos(\theta - \alpha_n) \cdot (\cos\theta, \sin\theta)$.

Owing to refraction across the inner shelf, wave angles are generally small in the surf zone, particularly for the larger (breaking) waves that contribute more heavily to the bias velocities; thus, $\partial\eta/\partial y \ll \partial\eta/\partial x$, and (13) takes the approximate form

$$\frac{\Delta r}{\Delta t} = \frac{-\frac{\partial \eta}{\partial t}}{\frac{\partial \eta}{\partial x}\cos\theta - \tan\tau} \tag{15}$$

except when $\theta \to \pi/2$. In this case, the look angle is directly down the coastline parallel to, and very near, the shoreline where η is small and $\alpha_n \approx 0$; thus, $\partial\eta/\partial y \cdot \sin\theta$ contributes negligibly to the bias. In order to arrive at a first-order analytical solution to the mean bias velocity, we will further assume that

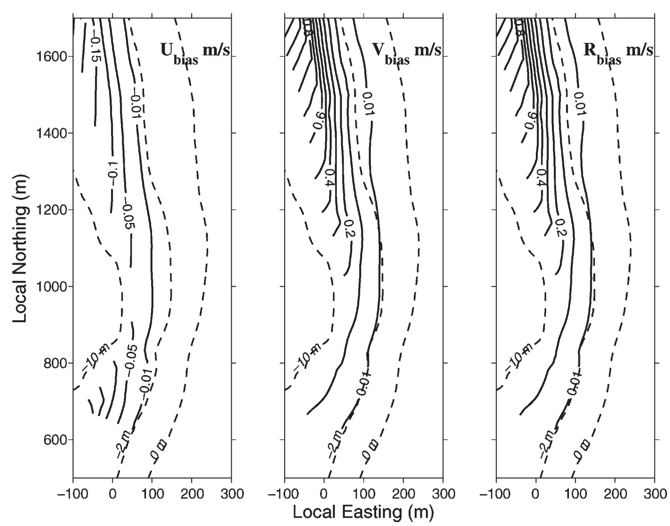

Fig. 13. (Solid lines) Contours of mean bias corrections from October 31, 2003, at NCEX for (left) cross-shore, (center) longshore, and (right) radially aligned currents. Also shown are (dashed lines) the 0-, 2-, and 10-m-depth contours.

the wave field is defined by a narrow spectral peak defined by a single sinusoidal wave propagating directly onshore ($\alpha = 0$) with amplitude a, wavenumber k, and peak radian frequency σ; thus, (15) becomes

$$\frac{\Delta r}{\Delta t} = \frac{\sigma}{k\cos\theta}\left(\frac{\sin(kx - \sigma t)}{\sin(kx - \sigma t) + \frac{\tan\tau}{ak\cos\theta}}\right). \tag{16}$$

The mean bias velocity $\Delta\bar{r}/\Delta t$ is found when (16) is phase averaged over a wave period to yield

$$\frac{\bar{\Delta} r}{\Delta t} = \frac{\sigma}{k\cos\theta}\left(1 - \frac{1}{\left(1 - \frac{a^2k^2\cos^2\theta}{\tan^2\tau}\right)^{1,2}}\right). \tag{17}$$

In order to use this formula in practice, an estimate is needed for the wave amplitude, frequency, and wavenumber of the approximately (assumed) shore-normally propagating narrow-banded wave field. In general, the wave frequency is assumed known (obtained by other means), and the wavenumber and amplitude are approximated by the shallow water dispersion relation (with amplitude dispersion) and surf similarity considerations

$$\begin{aligned} c &= \frac{\sigma}{k} = (gh(1+\gamma))^{1,2}\\ a &= \frac{1}{2}\gamma h \end{aligned} \tag{18}$$

where γ is a constant, g is the gravity, and h is the water depth. The mean cross-shore $U_{\rm bias}$ and alongshore $V_{\rm bias}$ bias velocities are then given by

$$U_{\rm bias} = \frac{\bar{\Delta} r}{\Delta t}\cos\theta \qquad V_{\rm bias} = \frac{\bar{\Delta} r}{\Delta t}\sin\theta. \tag{19}$$

As an example, using the measured bathymetry obtained at NCEX from October 30 to November 2, 2003, a peak wave period of 7.14 s and $\gamma = 0.32$ mean bias velocities are shown in Fig. 13 for the camera deployment geometry used during

NCEX for the data presented in this paper. The free parameter γ roughly accounts for truncating the Fourier representation of the wave field and should be verified in the field if at all possible. For this calculation, the value of 0.32 is taken as reasonable for a narrow-banded wave field at the site [55], [56]. In any case, the effect of γ on the bias is negligible when the tilt angle becomes large.

ACKNOWLEDGMENT

The authors would like to thank M. Okihiro and W. Pawlek of SIO (NCEX coordinator) for the assistance in all logistical areas; G. Farquharson, Z. Tulu, M. Behn, and E. Knapp of UMass for installing and operating the radar systems; and J. Shore, G. Smith, J. Magalen, J. Long, and D. Welsh for helping in collecting the video data. The video cameras mounted on the NOAA Southwest Fishery Science Center building are part of Oregon State University's Argus program headed by R. A. Holman.

REFERENCES

[1] R. T. Guza and E. B. Thornton, "Observations of surf beat," *J. Geophys. Res.*, vol. 90, no. C4, pp. 3161–3172, 1985.
[2] W. E. Schmidt, B. T. Woodward, K. S. Millikan, R. T. Guza, B. Raubenheimer, and S. Elgar, "A GPS-tracked surf zone drifter," *J. Atmos. Ocean. Technol.*, vol. 20, no. 7, pp. 1069–1075, Jul. 2003.
[3] T. C. Lippmann and R. A. Holman, "Quantification of sand bar morphology: A video technique based on wave dissipation," *J. Geophys. Res.*, vol. 94, no. C1, pp. 995–1011, Jan. 1989.
[4] R. A. Holman, A. H. Sallenger, T. C. Lippmann, and J. W. Haines, "The application of video image processing to the study of nearshore processes," *Oceanography*, vol. 6, no. 3, pp. 78–85, 1993.
[5] T. Aagaard and J. Holm, "Digitization of wave run-up using video records," *J. Coast. Res.*, vol. 5, no. 3, pp. 547–551, 1989.
[6] T. C. Lippmann and R. A. Holman, "Phase speed and angle of breaking waves measured with video techniques," in *Proc. Coastal Sediments*, N. C. Kraus, K. J. Gingerich, and D. L. Kriebel, Eds., 1991, pp. 542–556.
[7] F. Stockdon and R. Holman, "Estimation of wave phase speed and nearshore bathymetry from video imagery," *J. Geophys. Res.*, vol. 105, no. C9, pp. 22 015–22 033, Sep. 2000.
[8] C. Chickadel, R. Holman, and M. Freilich, "An optical technique for the measurement of longshore currents," *J. Geophys. Res.*, vol. 108, no. C11, pp. 28.1–28.17, Nov. 2003.
[9] T. C. Lippmann and R. A. Holman, "The spatial and temporal variability of sand bar morphology," *J. Geophys. Res.*, vol. 95, no. C7, pp. 11 575–11 590, Jul. 1990.
[10] T. C. Lippmann, R. A. Holman, and K. K. Hathaway, "Episodic, nonstationary behavior of a double bar system at duck, North Carolina, USA, 1986–1991," *J. Coast. Res.*, vol. 15, pp. 49–75, 1993.
[11] N. G. Plant and R. A. Holman, "Intertidal beach profile estimation using video images," *Mar. Geol.*, vol. 140, no. 1, pp. 1–24, Jul. 1997.
[12] R. A. Holman, T. C. Lippmann, P. V. O'Neill, and K. Hathaway, "Video estimation of subaerial beach profiles," *Mar. Geol.*, vol. 97, no. 1/2, pp. 225–231, 1991.
[13] S. G. J. Aarninkhof, B. Ruessnik, and J. A. Roelvink, "Nearshore subtidal bathymetry from time-exposure video images," *J. Geophys. Res.*, vol. 110, no. C6, p. C06 011, Jun. 2005.
[14] S. G. J. Aarninkhof and B. Ruessnik, "Video observations and model predictions of depth-induced wave dissipation," *IEEE Trans. Geosci. Remote Sens.*, vol. 42, no. 11, pp. 2612–2622, Nov. 2004.
[15] R. J. Adrian, "Twenty years of particle image velocimetry," *Exp. Fluids*, vol. 39, no. 2, pp. 159–169, Aug. 2005.
[16] K. Holland, J. Puleo, and T. Kooney, "Quantification of swash flows using video-based particle image velocimetry," *Coast. Eng.*, vol. 44, no. 2, pp. 65–77, Dec. 2001.
[17] D. E. Barrick, D. R. Thompson, and R. E. Carande, "First-order theory and analysis of MF/HF/VHF scatter from the sea," *IEEE Trans. Antennas Propag.*, vol. AP-20, no. 1, pp. 2–10, Jan. 1972.
[18] R. H. Stewart and J. W. Joy, "HF radio measurements of surface currents," *Deep Sea Res.*, vol. 21, pp. 1039–1049, 1974.
[19] D. M. Fernandez, J. F. Vesecky, and C. C. Teague, "Measurements of upper ocean surface current shear with high-frequency radar," *J. Geophys. Res.*, vol. 101, no. C12, pp. 28 615–28 625, 1996.
[20] I. R. Young, W. Rosenthal, and F. Ziemer, "A three-dimensional analysis of marine radar images for the determination of ocean wave directionality and surface currents," *J. Geophys. Res.*, vol. 90, no. C1, pp. 1049–1059, 1985.
[21] F. Ziemer and W. Rosenthal, "Directional spectra from ship-board navigation radar during LEWEX," in *Directional Ocean Wave Spectra: Measuring, Modeling, Predicting and Applying*, R. C. Beal, Ed. Baltimore, MD: The John Hopkins Univ. Press, 1991, pp. 125–127.
[22] C. M. Senet, J. Seemann, and F. Ziemer, "The near-surface current velocity determined from image sequences of the sea surface," *IEEE Trans. Geosci. Remote Sens.*, vol. 39, no. 3, pp. 492–505, Mar. 2001.
[23] J. C. Nieto Borge, G. R. Rodrigues, K. Hessner, and P. I. Gonzales, "Inversion of marine radar images for surface wave analysis," *J. Atmos. Ocean. Technol.*, vol. 21, no. 8, pp. 1291–1300, Aug. 2000.
[24] P. S. Bell, "Shallow water bathymetry derived from an analysis of X-band marine radar images of waves," *Coast. Eng.*, vol. 37, no. 3/4, pp. 513–527, Aug. 1999.
[25] S. J. Frasier and R. E. McIntosh, "Observed wavenumber-frequency properties of microwave backscatter from ocean surface at near-grazing angles," *J. Geophys. Res.*, vol. 101, no. C8, pp. 18 391–18 407, 1996.
[26] D. Moller, S. J. Frasier, D. L. Porter, and R. E. McIntosh, "Radar-derived interferometric surface currents and their relationship to subsurface current structure," *J. Geophys. Res.*, vol. 103, no. C6, pp. 12 839–12 852, 1998.
[27] R. M. Goldstein, T. P. Barnett, and H. A. Zebker, "Remote sensing of ocean currents," *Science*, vol. 246, no. 4935, pp. 1282–1285, Dec. 1989.
[28] H. C. Graber, D. R. Thompson, and R. E. Carande, "Ocean surface features and currents measured with synthetic aperture radar interferometry and HF radar," *J. Geophys. Res.*, vol. 101, no. C11, pp. 25 813–25 832, Nov. 1996.
[29] J. A. Puleo, G. Farquharson, S. J. Frasier, and K. T. Holland, "Comparison of optical and radar measurements of surf and swash zone velocity fields," *J. Geophys. Res.*, vol. 108, no. C3, p. 3100, Mar. 2003. DOI: 10.1029/2002JC001483.
[30] G. Farquharson, S. J. Frasier, B. Raubenheimer, and S. Elgar, "Microwave radar cross sections and Doppler velocities measured in the surf zone," *J. Geophys. Res.*, vol. 110, no. C12, p. C12 024, Dec. 2005.
[31] G. Farquharson, M. Behn, D. Perkovic, Z. Culcuoglu, and S. J. Frasier, "Microwave radar remote sensing of surface currents in the nearshore region," in *Proc. IGARSS*, Anchorage, AK, 2004, vol. 2, pp. 1160–1163.
[32] K. T. Holland, R. A. Holman, T. C. Lippmann, J. Stanley, and N. Plant, "Practical use of video imagery in nearshore oceanographic field studies," *IEEE J. Ocean. Eng.*, vol. 22, no. 1, pp. 81–92, Jan. 1997.
[33] J. W. Wright, "A new model for sea clutter," *IEEE Trans. Antennas Propag.*, vol. AP-16, no. 2, pp. 217–223, Mar. 1968.
[34] W. J. Plant, "The modulation transfer function: Concept and applications," in *Radar Scattering From Modulated Wind Waves*, G. J. Komen and W. A. Oost, Eds. Norwell, MA: Kluwer, 1989, pp. 155–172.
[35] W. J. Plant, "Bragg scattering of the electromagnetic waves from air/sea interface," in *Surface Waves and Fluxes*, G. Greenaert and W. J. Plant, Eds. Norwell, MA: Kluwer, 1990, pp. 41–108.
[36] B. L. Lewis and I. D. Olin, "Experimental study and theoretical model of high-resolution radar backscatter from the sea," *Radio Sci.*, vol. 15, no. 4, pp. 815–828, Jul./Aug. 1980.
[37] L. Wetzel, "On microwave scattering by breaking waves," in *Wave Dynamics and Radio Probing of the Sea Surface*. New York: Plenum, 1986, pp. 273–284.
[38] S. J. Frasier, Y. Liu, R. E. McIntosh, and C. Long, "Space-time properties of radar sea spikes and their relation to wind and wave conditions," *J. Geophys. Res.*, vol. 103, no. C9, pp. 18 745–18 757, Aug. 1998.
[39] P. H. Y. Lee, J. D. Barter, K. L. Beach, B. M. Lake, H. Rungaldier, H. R. Thompson, L. Wang, and R. Yee, "What are the mechanisms for non-Bragg scattering from water wave surfaces?" *Radio Sci.*, vol. 34, no. 1, pp. 123–138, 1999.
[40] M. A. Sletten, J. C. West, X. Liu, and J. H. Duncan, "Radar investigations of breaking water waves at low grazing angles with simultaneous high-speed optical imagery," *Radio Sci.*, vol. 38, no. 6, p. 1110, Dec. 2003. DOI: 10.1029/2002RS002716.
[41] W. C. Keller, T. R. Larson, and J. W. Wright, "Mean speeds of wind waves at short fetch," *Radio Sci.*, vol. 12, pp. 1091–1100, Dec. 1974.

[42] W. C. Keller, W. J. Plant, and G. R. Valenzuela, "Observations of breaking ocean waves with coherent microwave radar," in *Wave Dynamics and Radio Probing of the Sea Surface*. New York: Plenum, 1986, pp. 285–293.
[43] A. T. Jessup and W. K. Melville, "Breaking waves affecting microwave backscatter 1. Detection and verification," *J. Geophys. Res.*, vol. 96, no. C11, pp. 20 547–20 559, Nov. 1991.
[44] M. C. Haller and D. R. Lyzenga, "Comparison of radar and video observations of shallow water breaking waves," *IEEE Trans. Geosci. Remote Sens.*, vol. 41, no. 4, pp. 832–844, Apr. 2003.
[45] K. S. Miller and M. M. Rochwarger, "A covariance approach to spectral moment estimation," *IEEE Trans. Inf. Theory*, vol. IT-18, no. 5, pp. 588–596, Sep. 1972.
[46] S. K. Misra, A. B. Kennedy, and J. T. Kirby, "An approach to determining nearshore bathymetry using remotely sensed ocean surface dynamics," *Coast. Eng.*, vol. 47, no. 3, pp. 265–293, Jan. 2003.
[47] G. Roth, D. Hart, and J. Katz, "Feasibility of using the l64720 video motion estimation processor (MEP) to increase efficiency of velocity map generation for particle image velocimetry (PIV)," in *Proc. Fluids Eng. Laser Anemometry Conf. Exhib.*, 1995, pp. 1–7.
[48] M. Raffel, C. E. Willert, and J. Kompenhans, *Particle Image Velocimetry: A Practical Primer*. Berlin, Germany: Springer-Verlag, 1998.
[49] N. G. Plant, K. T. Holland, and J. A. Puleo, "Analysis of the scale of errors in nearshore bathymetric data," *Mar. Geol.*, vol. 191, no. 1, pp. 71–86, Nov. 2002.
[50] D. R. Thompson and J. R. Jensen, "Synthetic aperture radar interferometry applied to ship-generated internal waves in the 1989 Loch Linnhe experiment," *J. Geophys. Res.*, vol. 98, no. C6, pp. 10 259–10 269, Jun. 1993.
[51] J. C. Church and E. B. Thornton, "Effects of breaking wave induced turbulence within a longshore current model," *Coast. Eng.*, vol. 20, no. 1/2, pp. 1–28, Jul. 1993.
[52] B. G. Ruessink, J. R. Miles, F. Feddersen, R. T. Guza, and S. Elgar, "Modeling the alongshore current on barred beaches," *J. Geophys. Res.*, vol. 106, no. C10, pp. 22 451–22 464, 2001.
[53] F. Feddersen and R. T. Guza, "Observations of nearshore circulation: Alongshore uniformity," *J. Geophys. Res.*, vol. 108, no. C1, pp. 1–6, Jan. 2003.
[54] R. Holman, J. Stanley, and T. Ozkan-Haller, "Applying video sensor networks to nearshore environmental monitoring," *Pervasive Comput.*, vol. 2, no. 4, pp. 14–21, Oct.–Dec. 2003.
[55] T. C. Lippmann, A. H. Brookins, and E. B. Thornton, "Wave energy transformation on natural profiles," *Coast. Eng.*, vol. 27, no. 1/2, pp. 1–20, May 1996.
[56] B. Raubenheimer, R. T. Guza, and S. Elgar, "Wave transformations in the inner surf zone," *J. Geophys. Res.*, vol. 101, pp. 25 589–25 597, 1996.

Dragana Perkovic (M'00) received the B.S. degree in electrical engineering from the University of Malta, Msida, Malta, in 2002, and the Ph.D. degree from the University of Massachusetts, Amherst, in 2008.

She joined the Microwave Remote Sensing Laboratory, University of Massachusetts, in August 2003, where her graduate work focused on nearshore ocean applications using ground-based pulsed Doppler radar, as well as airborne dual-beam interferometric synthetic aperture radar. She is currently with the Radar Science and Engineering Department, Jet Propulsion Laboratory, Pasadena, CA.

Thomas C. Lippmann received the B.A. degree in mathematics and biology from Linfield College, McMinnville, OR, in 1985, and the M.S. and Ph.D. degrees in oceanography from Oregon State University, Corvallis, in 1989 and 1992, respectively.

From 1992 to 1995, he was a National Research Council Postdoctoral Fellow with the Department of Oceanography, Naval Postgraduate School, Monterey, CA. From 1995 to 2003, he was a Research Oceanographer with the Center for Coastal Studies, Scripps Institution of Oceanography, University of California, San Diego, La Jolla, and from 1999 to 2008, he was a Research Scientist with the Byrd Polar Research Center, The Ohio State University, Columbus. In 2008, he moved to the Center for Coastal and Ocean Mapping, University of New Hampshire, Durham, where he is currently a Research Associate Professor with the Department of Earth Sciences and Ocean Engineering. His research interests include nearshore physical oceanography, sediment transport, large-scale coastal behavior, and field methods in shallow marine environments, including applications with land and airborne video systems and acoustic echosounders aboard small vessels.

Dr. Lippmann is a member of the American Geophysical Union, the Oceanography Society, and the American Society of Civil Engineers.

Stephen J. Frasier (SM'03) received the B.E.E. degree from the University of Delaware, Newark, in 1987 and the Ph.D. degree from the University of Massachusetts, Amherst, in 1994.

From 1987 to 1990, he was with SciTec, Inc., Princeton, NJ (a subsidiary of TRW), analyzing the electromagnetic and optical signatures of rocket plumes, evaluating laser detection systems, and developing data acquisition systems supporting airborne infrared sensors. In August 1990, he joined the Microwave Remote Sensing Laboratory, Department of Electrical and Computer Engineering, University of Massachusetts, where his graduate work involved the development and application of digital-beamforming phased-array radar for oceanographic research applications. Since 1997, he has been a Faculty Member at the University of Massachusetts, where he is currently a Professor and the Director of the Microwave Remote Sensing Laboratory, Department of Electrical and Computer Engineering. His research interests include microwave imaging and interferometric techniques, radar oceanography, and radar meteorology. He currently leads radar research programs studying surface waves and currents in the ocean and studying winds and turbulence in the lower atmosphere.

Dr. Frasier is a member of the IEEE Geoscience and Remote Sensing Society, URSI Commission F, the American Geophysical Union, and the American Meteorological Society.